CHEMISTRY OF MATERIALS
Article

Chem. Mater. **2010,** *22,* 4083–4089 4083
DOI:10.1021/cm100866g

One-Step Preparation of SnO_2 and Pt-Doped SnO_2 As Inverse Opal Thin Films for Gas Sensing

Massimiliano D'Arienzo,*[,†] Lidia Armelao,[‡] Adriana Cacciamani,[†] Claudio Maria Mari,[†] Stefano Polizzi,[§] Riccardo Ruffo,[†] Roberto Scotti,[†] Andrea Testino,[†] Laura Wahba,[†] and Franca Morazzoni[†]

[†]*INSTM, Department of Materials Science, University of Milano-Bicocca, Via R. Cozzi 53, I-20125 Milano, Italy,* [‡]*ISTM−CNR and INSTM, Department of Chemical Sciences, University of Padova, Via F. Marzolo 1, I-35131 Padova, Italy., and* [§]*Department of Physical Chemistry, University of Venezia, Via Torino 155/b, I-30172 Venezia, Italy*

Received March 26, 2010. Revised Manuscript Received May 14, 2010

A new, fast, one-pot synthesis of SnO_2 and Pt−doped SnO_2 inverted opal thin films, to be used as materials for gas sensing, was carried out. Films were built from crystalline cassiterite nanoparticles, uniform in size (∼5 nm), resulting in a well-organized hierarchical structure of macro- and mesopores. The noble metal was homogeneously dispersed into the sensing layer of the oxide and the doping centers were present as Pt(IV) and Pt(II) species, partially reduced to Pt(0) after the interaction with the reducing gas (CO). The values of the electrical sensitivity under CO/Air atmosphere demonstrated that the response of Pt-doped films is higher than that of bare SnO_2 films, and that the response of inverted opal films is higher compared to that of the sol−gel films. The regular array of cassiterite nanoparticles, strongly interconnected and ordered as close-packed hollow spheres, promotes the effective gas diffusion through the oxide layer and, along with the electron acceptor ability of Pt(IV) doping centers, significantly contributes to enhancing the electrical sensitivity. The conductance regime of the Pt-doped SnO_2 inverted opal film is indicative of a regular microstructure of SnO_2 nanoparticles.

1. Introduction

The preparation and the functional properties of oxide semiconductor-based gas sensors, obtained by using hierarchical/hollow oxide nanostructures, were recently reviewed by Lee.[1] A relevant number of synthetic strategies were reported as well as the parameters related to the sensing characteristics of the materials.

The high surface area of these nanostructured materials provides high gas sensitivity because of their surface, which is readily accessible to the analyte molecules. At the same time, the porous structure, e.g., the opal structure,[2] hollow spheres,[3] nanoflowers,[4] and nanotubes,[5] offers favorable kinetics and fast-responding sensing behaviors.

Although a designed morphology seems to be very important in inducing strong and fast electrical response, an equally important aspect is to investigate to what extent the chemical doping by noble metal atoms enhances the electrical response of oxide hierarchical nanostructures.[6] Our group recently reported that the doping of tin oxide films by noble metals (e.g., Pt) enhances the electrical response under CO treatment, according to the following equilibria[7]

$$O_O + CO \leftrightarrows CO_2 + V_O \quad (1)$$

$$V_O \leftrightarrows V_O^{\bullet} + e^- \quad (2)$$

$$Pt^{4+} + nV_O^{\bullet} \leftrightarrows Pt^{(4-n)+} + nV_O^{\bullet\bullet} \quad (3)$$

*Corresponding author. E-mail: massimiliano.darienzo@mater.unimib.it.

(1) Lee, J. H. *Sens. Actuators, B* **2009**, *140*, 319.
(2) (a) Scott, R. W. J.; Yang, S. M.; Chabanis, G.; Coombs, N.; Williams, D. E.; Ozin, G. A. *Adv. Mater.* **2001**, *13*, 1468. (b) Scott, R. W. J.; Yang, S. M.; Coombs, N.; Williams, D. E.; Ozin, G. A. *Adv. Funct. Mater.* **2003**, *13*, 225. (c) Acciarri, M.; Barberini, R.; Canevali, C.; Mari, C. M.; Mattoni, M.; Morazzoni, F.; Nodari, L.; Polizzi, S.; Ruffo, R.; Russo, U.; Sala, M.; Scotti, R. *Chem. Mater.* **2005**, *17*, 6167. (d) Sutti, A.; Baratto, C.; Calestani, G.; Dionigi, C.; Ferroni, M.; Faglia, G.; Sberveglieri, G. *Sens. Actuators, B* **2008**, *130*, 567. (e) Sasahara, K; Hyodo, T.; Shimizu, Y.; Egashira, M. *J.Eur. Ceram. Soc.* **2004**, *24*, 1961.
(3) (a) Chang, Y. E.; Youn, D. Y.; Ankonina, G.; Yang, D. J.; Kim, H. G.; Rothschild, A.; Kim, I. D. *Chem.Comm.* **2009**, 4019. (b) Kim, H. R.; Choi, K. I.; Lee, J. H.; Akbar, S. A. *Sens. Actuators, B* **2009**, *136*, 138. (c) Wang, H.; Liang, J.; Fan, H.; Xi, B.; Zhang, M.; Xiong, S.; Zhu, Y.; Qian, Y. *J. Solid State Chem.* **2008**, *181*, 122. (d) Tan, Y.; Li, C.; Wang, Y.; Tang, J.; Ouyang, X. *Thin Solid Films* **2008**, *516*, 7840.
(4) (a) Jiang, L. J.; Wu, X. L.; Guo, Y. G.; Wan, L. J. *J.Phys.Chem. C* **2009**, *113*, 14213. (b) Firooz, A. A.; Mahjoub, A. R.; Khodadadi, A. A. *Mater. Chem. Phys.* **2009**, *115*, 196. (c) Firooz, A. A.; Mahjoub, A. R.; Khodadadi, A. A. *Sens. Actuators, B* **2009**, *141*, 89.
(5) (a) Dong, Q.; Su, H.; Xu, J.; Zhang, D. *Sens. Actuators, B* **2007**, *123*, 420–428. (b) Jia, Y; He, L.; Guo, Z.; Chen, X.; Meng, F.; Luo, T.; Li, M.; Liu, J. *J. Phys.Chem, C* **2009**, *113*, 9581.
(6) (a) Lee, Y. C.; Huang, H.; Tan, O. K.; Tse, M. S. *Sens. Actuators, B* **2008**, *132*, 239–242. (b) Yuasa, M.; Masaki, T.; Kida, T.; Shimanoe, K.; Yamazoe, N. *Sens. Actuators, B* **2009**, *136*, 99.
(7) (a) Morazzoni, F.; Canevali, C.; Chiodini, N.; Mari, C. M.; Ruffo, R.; Scotti, R.; Armelao, L.; Tondello, E.; Depero, L. E.; Bontempi, E. *Chem. Mater.* **2001**, *13*, 4355. (b) Armelao, L.; Barreca, D.; Bontempi, E.; Canevali, C.; Depero, L. E.; Mari, C. M.; Ruffo, R.; Scotti, R.; Tondello, E.; Morazzoni, F. *Appl. Magn. Reson.* **2002**, *22*, 89. (c) Acciarri, M.; Canevali, C.; Mari, C. M.; Mattoni, M.; Ruffo, R.; Scotti, R.; Morazzoni, F.; Armelao, L.; Barreca, D.; Tondello, E; Bontempi, E.; Depero, L. E. *Chem. Mater.* **2003**, *15*, 2646. (d) Morazzoni, F.; Canevali, C.; Chiodini, N.; Mari, C.; Ruffo, R.; Scotti, R.; Armelao, L.; Tondello, E.; Depero, L. E.; Bontempi, E. *Mater. Sci. Eng. C* **2001**, *15*, 167.

Published on Web 05/28/2010

where O_O is the oxide anion in a regular oxygen site, V_O is the neutral oxygen vacancy, $V_O^{\bullet}$ the singly ionized oxygen vacancy, and $V_O^{\bullet\bullet}$ is the doubly ionized oxygen vacancy ($n = 2, 4$ for Pt).

The change in oxidation state of noble metal centers, described in reaction 3, shifts to the right to release electrons in reaction 2 and ultimately favors the production of V_O defects (reaction 1), increasing the number of electrons injected into the conduction band with respect to undoped SnO_2. It is expected that the easier the metal reduction (reaction 3), the easier the transfer of electrons to the conduction band (reaction 2), and the higher the noble metal oxidation state (reaction 3), the stronger the electrical response.

Nevertheless, noble metal doping of hierarchically structured oxide materials remains a challenge, mainly because of the difficulty of obtaining significant and homogeneous dispersions of the dopant species into the oxide lattice. In fact, physical methods generally lead to deposition of the metal at the oxide surface, resulting in a limited interface contact between the two phases. Moreover, they usually require very expensive equipments whose scale-up is not convenient.[8] A chemical method, such as the sol−gel procedure, in principle guarantees easy and homogeneous dispersion of the noble metal dopant, and involves the use of organic solvent/water mixtures suitable for both noble metal and tin precursors.[2d,9]

The present paper reports on the novel one-step preparation of SnO_2 and Pt-doped SnO_2 in the form of inverted opal films, obtained by sol−gel synthesis and dip coating deposition. The process uses a colloidal solution of the oxide precursor into an aqueous suspension of polystyrene latex (PS) microspheres as the template agent, mixed with an ethanol solution of the Pt precursor. The procedure simultaneously allows the self-assembled formation of the close-packed PS array and the simultaneous infiltration of the precursors into the voids of the structure. The oxide solid skeleton around the spheres was obtained in one-step, at variance to the conventional two-step process based on the infiltration into the preformed self-assembled PS array.[2]

The method is easy to apply and fast to produce hierarchically ordered nanoscale structures. Furthermore, it allows doping by addition of the noble metal precursor to the starting aqueous solution, dissolved in the minimum amount of ethanol. Some authors reported on template-assisted, one-step preparations of inverted opal structured oxides;[10] however, to the best of our knowledge, the doping of the SnO_2 film by noble transition metals, which are able to greatly improve the electric response (see results), has never been achieved by this route.

The morphology of the tin oxide films and the electronic properties of the doping centers were also investigated, in order to suggest a mechanism explaining the high sensitivity toward CO/air gas mixtures. The electrical response and sensitivity of the inverted opal films were examined and compared to those of conventional nanostructured sol−gel films, with the aim to investigate the relative importance of the noble metal doping and the hierarchical nanostructure in affecting the electrical behaviour.

2. Experimental Section

2.1. Chemicals. The colloidal suspensions of polystyrene (PS) latex microspheres (ca. 300 nm ∅) in water (2.5 wt %) were purchased from DistriLab. Tetrakis(tert-butoxy)tin(IV), $[Sn(OBu^t)_4]$, tin tetrachloride $[SnCl_4 \cdot 5H_2O]$, and bis(acetylacetonate)platinum-(II) $[Pt(acac)_2]$ were Aldrich pure chemicals and used as-received.

2.2. Preparation of Precursor Suspensions for Inverted Opal Film Deposition of Undoped and Pt-Doped SnO_2. SnO_2 precursor suspension was prepared by dissolving 0.5 g of $SnCl_4 \cdot 5H_2O$ in 5 mL of the colloidal aqueous suspension of PS latex microspheres. The mixture obtained was stirred at room temperature for several minutes until a homogeneous suspension was obtained. (Pt)-doped SnO_2 precursor suspension (Pt:Sn molar ratio 0.025) was prepared by simply adding the proper amount of $[Pt(acac)_2]$ dissolved in the minimum quantity of anhydrous ethanol ($\sim$ 1.2 mL) to the SnO_2 precursor suspension.

2.3. Preparation of Precursor Solutions for Deposition of Undoped and Pt-Doped SnO_2 Sol−Gel Films. According to the method previously reported,[7c,11] the noble metal precursor solution was obtained by dissolving 0.1064 g of $[Pt(acac)_2]$ in 15 mL of an anhydrous ethanol−acetylacetone solution (1:1 v:v).

A second solution was prepared by mixing under a dry atmosphere (nitrogen): (i) 2.50 mL of a solution of $[Sn(OBu^t)_4]$ (360 mg mL^{-1}) in anhydrous ethanol−acetylacetone (3.85:1 v:v; corresponding to 2.19 mmol of Sn); (ii) 3.00 mL of the Pt precursor solution (corresponding to 5.47×10^{-2} mmol of metal; Pt:Sn molar ratio 0.025).

The sol phase was obtained by further adding 1.00 mL of an ethanol−water solution (4:1 v:v; corresponding to 11.1 mmol of H_2O), 1.52 mL of ethanol, and 0.48 mL of acetylacetone to the previous solution.

The sol phase of undoped SnO_2 was obtained by the same procedure, adding 3 mL of ethanol instead of the noble metal precursor solution.

The solutions were transferred into a capillary viscosimeter and kept in a thermostatic chamber at 35 ± 1 °C. After 24 h, 0.10 mL of ethanol−water solution (4:1 v:v; corresponding to 1.11 mmol of H_2O) was further introduced; the addition was repeated every 24 h until the sol-phase viscosity became 2.5 cSt, a suitable value for the dip-coating deposition.

2.4. Inverted Opal Film Deposition. The inverted opal films were prepared by a novel one-pot procedure using the dip-coating method.

Alumina slides (20 × 20 mm, 0.25 mm thickness) or Suprasil quartz slides were similarly used as substrates.

In a typical deposition, the substrate was placed vertically into the SnO_2/PS or the Pt-doped SnO_2/PS sol phase for several minutes and then withdrawn at a constant rate of 0.8 cm/min. The procedure allows the self-assembly of the close-packed PS

(8) (a) Ivanov, P.; Llobet, E.; Vilanova, X.; Brezmes, J.; Hubalek, J.; Correig, X. *Sens. Actuators, B* **2004**, *99*, 201. (b) Colina, J. Z.; Nix, R. M. *Surf. Sci.* **2006**, *600*, 3058. (c) Gaidi, M.; Chenevier, B.; Labeau, M.; Hazemann, J. L. *Sens. Actuators, B* **2006**, *120*, 313. (d) Salehi, A.; Gholizade, M. *Sens. Actuators, B* **2003**, *89*, 173.
(9) Leitea, E. R.; Bernardi., M. I. B.; Longo, E.; Varela, J. A.; Paskocimas, C. A. *Thin Solid Films* **2004**, *449*, 67.
(10) (a) Subramanian, G.; Manoharan, V. N.; Thorne, J. D.; Pine, D. J. *Adv. Mater.* **1999**, *11*, 1261. (b) Meng, Q.-B.; Fu, C.-H.; Einaga, Y.; Gu, Z.-Z.; Fujishima, A.; Sato, O. *Chem. Mater.* **2002**, *14*, 83.
(11) Scotti, R.; Canevali, C.; Mattoni, M.; Morazzoni, F.; Armelao, L.; Barreca, D. Nanostructured Pt-doped tin oxide films. In *Materials Syntheses*; Schubert, U., Hüsing, N., Laine, R., Eds.; Springer: New York, 2008; p 117.

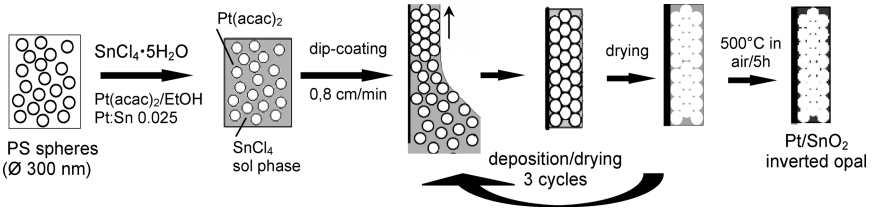

Figure 1. Schematic of one-step preparation of inverted opal films.

array, acting as the template, and the simultaneous infiltration of the precursor suspension into the PS structure. The diameter of PS spheres was chosen among those suitable to obtain close-packed arrays, typically between 90 and 500 nm. After the deposition, the films were dried in air for about 10 min at 60 °C. The above cycle was repeated three times and then the films were annealed at 500 °C (heating rate 2 °C min^{-1}) in air stream (80 cm^3 min^{-1}) for 5 h, in order to fully decompose the PS template. In depth XPS analysis (see section 3.2) showed no residual organic contaminants in the films, and that the Pt/Sn atomic ratio is ~0.006, i.e. about one-fourth of the nominal value. This result suggests that only a part of the noble metal precursor dissolved in the sol phase is actually embedded in the colloidal tin oxide nanoparticles.

The scheme of the one-step deposition method is reported in Figure 1.

2.5. Sol−Gel Film Deposition. Sol−gel films were deposited in air by dip-coating (0.8 cm/min), dried at room temperature, and then annealed at 400 °C in air stream (80 cm^3 min^{-1}) for 2 h. The thermal treatment fully decomposed the acetylacetonate ligand, and no residual organic contaminants remained in the film, as assessed by the in depth XPS analysis.[7c,11]

Films were obtained by means of three successive depositions. A final thermal treatment was carried out at 500 °C (heating rate 2 °C min^{-1}) in an air stream (80 cm^3 min^{-1}) for 5 h.

2.6. Morphological and Chemical Characterization. Film morphology was analyzed by scanning electron microscopy (SEM) using a Vega TS5136 XM Tescan microscope in a high-vacuum configuration. The electron beam excitation was 30 kV at a beam current of 25 pA, and the working distance was 12 mm. In this configuration, the beam spot was 38 nm. Prior to the SEM analysis, samples were gold-sputtered.

High-resolution transmission electron microscopy (HRTEM) analyses were performed at 300 kV using a JEOL 3010 apparatus with a high-resolution pole piece (0.17 nm point-to-point resolution), equipped with a Gatan slow-scan 794 CCD camera. Elemental composition was determined by an Oxford Instruments EDS microanalysis detector (model 6636). Samples were obtained by removing a film portion from the substrates in order to obtain a fine powder sample, then suspended in 2-propanol. A 5 μL drop of this suspension was deposited on a holey carbon film supported on a 3 mm copper grid for TEM investigation.

The surface chemical composition of the films was investigated by X-ray photoelectron spectroscopy. XPS analysis was performed on samples annealed in air stream (50 cm^3 min^{-1}) at 773 K and on those successively treated in CO (600 ppm)/Ar stream (50 cm^3 min^{-1}) at 623 K. Because of the equivalence of the electric behavior (see later), the samples deposited on Suprasil quartz slides were used for XPS analysis, in order to avoid possible interferences between Pt4f and Al2p peaks. Annealing treatments were performed in a quartz reactor and samples were directly transferred into the fast entry lock system of the XPS vacuum chamber in order to avoid surface modification or atmospheric contamination of the layers because of air exposure. The analysis was performed with a Perkin-Elmer Φ 5600-ci spectrometer using nonmonochromatized Al−K_α radiation (1486.6 eV). The sample analysis area was 800 μm in diameter and the working pressure was $< 1 \times 10^{-9}$ mbar. The spectrometer was calibrated by assuming the binding energy (BE) of the Au $4f_{7/2}$ line at 83.9 eV with respect to the Fermi level. The standard deviation for the BEs values was ±0.2 eV. Survey scans were obtained in the 0−1300 eV range. Detailed scans were recorded for the C1s, O1s, Sn3d, and Pt4f regions. No further element was detected, or signals from the silica substrate. The samples were sufficiently electrically conductive at room temperature that no compensation for charging effects was required. The residual BE shifts (on the order of ~0.5 eV) were corrected by assigning to the C1s peak associated with adventitious hydrocarbons a value of 284.8 eV. The analysis involved Shirley-type background subtraction, nonlinear least-squares curve fitting, adopting Gaussian−Lorentzian peak shapes and peak area determination by integration. The atomic compositions were evaluated from peak areas using sensitivity factors supplied by Perkin-Elmer, taking into account the geometric configuration of the apparatus. The experimental uncertainty on the reported atomic composition values does not exceed ±5%.

Depth profiles were carried out by Ar^+ sputtering at 2.5 kV with an argon partial pressure of $\sim 1 \times 10^{-8}$ mbar, and a rastered area of 2 × 2 mm^2. For each sample, the chemical composition was checked in at least three different areas.

2.7. Electrical Measurements. Before film deposition, alumina or Suprasil quartz slides were equipped with two gold current collectors (20 mm) deposited at a distance of about 3 mm from each other by the dc sputtering technique. The samples were then put in a quartz chamber placed in an oven, and the measurements were performed at different temperatures, ranging from 523 to 623 K. The electrical resistance was measured by a Keithley 617 programmable electrometer, and the data acquisition was controlled by a PC. A system based on volumetric gas mixing through mass flow controllers and certified bottles was used to dynamically reproduce environmental conditions in a controlled and repeatable way. The following sequence of treatments was adopted. The sensing element was equilibrated in air flow (100 mL min^{-1}) at the selected temperature, and then CO (72.5−580 ppm)/air mixture was introduced (100 mL min^{-1}) up to equilibrium conditions. The different gas mixtures were obtained by dilution of the initial CO(580 ppm)/air mixture using a mass flometer. The starting resistance conditions of the film were restored by air equilibration, before again introducing the CO/Air mixture. S is the electrical response defined as the ratio between the film resistance under flowing air, R_{air}, and under flowing CO/air mixture, R_{mix}, respectively ($S = R_{air}/R_{mix}$).

3. Results and Discussion

3.1. Morphological Investigation. The SEM investigation revealed that both undoped and Pt-doped SnO_2

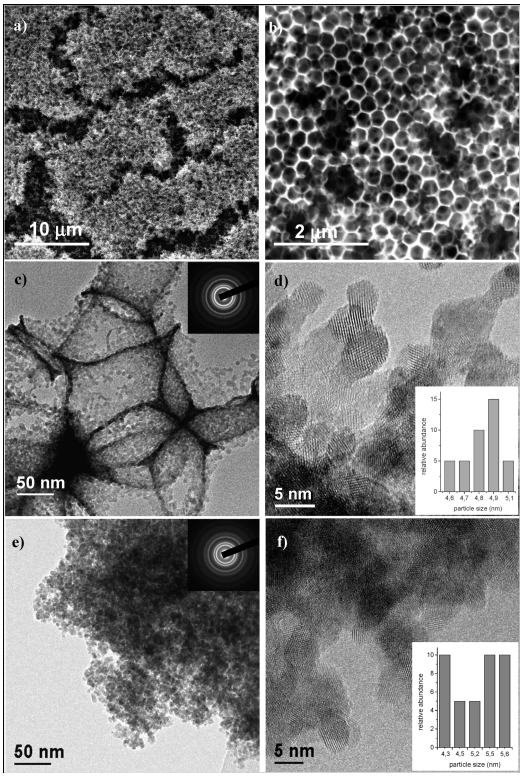

Figure 2. SEM (a, b) Micrographs of Pt-doped SnO_2 inverted opal films. (c, e) TEM and (d, f) HRTEM images of (c, d) Pt-doped SnO_2 inverted opal films and (e, f) Pt-doped SnO_2 sol−gel films. Insets in c and e report the ED patterns; rings correspond to tin oxide cassiterite phase. Insets in d and f report the particle-size distribution of cassiterite in Pt-doped SnO_2 inverted opal and Pt-doped SnO_2 sol−gel films. About 40 particles from four different sample regions were observed for inset plots in d and f.

based films (Figure 2a,b) exhibit the inverted opal structure. No pore occlusion was detectable. A double order porosity (mean $\varnothing = 250 \pm 5$ nm) due to macropores, resulting from the template structure, combined with mesopores (~30−40 nm from TEM images) and resulting from the contact among the PS spheres was observed. These results confirm that the one-step preparation, although very fast in comparison to the two-step deposition method, guarantees the formation of close-packed PS arrays and the simultaneous permeation of the precursor solution into the opal structure. After thermal annealing, a structure with satisfactory macroporous order and high permeability was obtained, constituted by a solid skeleton of tin oxide nanoparticles surrounding the hollow spheres. The oxide wall thickness was found to never exceed tens of nanometers.

The integrity of the whole structure was found to be substantially preserved during the thermal treatment. EDS investigations and SEM backscattered electron images demonstrated the homogeneous distribution of the different metal centers across the oxide layer. No metal clusters or secondary phases were observed: this confirms the homogeneous dispersion of the noble metal into the oxide matrix.

TEM and HRTEM images of some representative samples are reported in Figure 2c−f. No amorphous surface layers were detectable. In the case of Pt-doped SnO_2 inverted opal (Figure 2c,d), particles are constituted by cassiterite nanocrystals that build up the structure of the hollow spheres. Nanoparticles are highly interconnected and present a narrow size distribution (see inset in Figure 2d) centered around 5 nm (dimension comparable with the double of the Debye length, L_d). In principle these features should favor an optimal sensing behavior, due to extension of the depletion layer to the whole particle and short times of electron transfer. Sol−gel cassiterite nanoparticles (Figure 2e, f) present a similar size distribution (centered between 4 and ~6 nm); however, they are irregularly organized in large aggregates because of the absence of macroporosity.

3.2. XPS Investigation. XPS analysis was performed on inverted opal films annealed in an air stream at 773 K and subsequently treated in CO (600 ppm)/Ar stream at 623 K.

The binding energies (BE) values were measured for the Pt4f, Sn3d, O1s, and C1s lines.

A common feature observed for the films is the position of the main ($j = 5/2$) spin−orbit split component of the Sn3d peak at 487.0 eV, which is typical for Sn(IV) sites coordinated by oxygen atoms.[9,12] No variations in the Sn3d shape or position were observed after the thermal treatments, even under CO/Ar atmosphere, indicating that tin atoms in the SnO_2 matrix do not undergo reducing processes.

Regarding the O1s peak, a significant broadening and the presence of a shoulder on the high BE side are observed for all the samples, thus suggesting the coexistence of different chemical environments. After peak deconvolution (Figure 3a), the O1s spectra reveal splitting into two bands.

The major component at 530.9 eV is typical for the SnO_2 cassiterite network, whereas the second minor band at higher BE (ca. 532.5 eV) is mainly related to the presence of ≡Sn−OH species and/or to some surface hydration.[12,13] As a consequence, the corresponding O/Sn atomic ratio was ca. 2.5, which is higher than the stoichiometric value (i.e., 2) expected for the oxide.

Variations were instead observed in the Pt4f peak position and band shape, depending on processing conditions. In fact, after treatment under air stream at 773 K, both Pt(IV) (BE $Pt4f_{7/2} \approx 75.9$ eV, $j-j$ doublet separation of ca. 3 eV) and Pt(II) (BE $Pt4f_{7/2} \approx 72.7$ eV, $j-j$ doublet separation of ca. 2.9 eV) species were detected in the outer layers of the coatings,[12] with a relative Pt(II)/Pt(IV) atomic ratio of ca. 2 (Figure 3b). Instead, after treatment under CO (600 ppm)/Ar stream at 623 K, besides Pt(IV) (BE $Pt4f_{7/2} \approx 75.8$ eV, $j-j$ doublet separation ca. 2.9 eV) and Pt(II) centers (BE $Pt4f_{7/2} \approx 72.7$ eV, $j-j$ doublet separation ca. 2.8 eV), a different reduced platinum species (BE $Pt4f_{7/2} \approx 71.5$ eV, $j-j$ doublet separation ca. 3.0 eV) appeared, very close in energy to the zero-valence state[12] (Figure 3c). The relative amount between Pt(0)/Pt(II)/Pt(IV) species resulted 1/1.6/0.8.

(12) Moulder, J. F.; Stikle, W. F.; Sobol, P. E.; Bomben, K. D. *Handbook of X-Ray Photoelectron Spectroscopy*; Perkin Elmer Corp.: Eden Prairie, MN, 1992.
(13) Kelly, R. *Surf. Sci.* **1980**, *100*, 85.

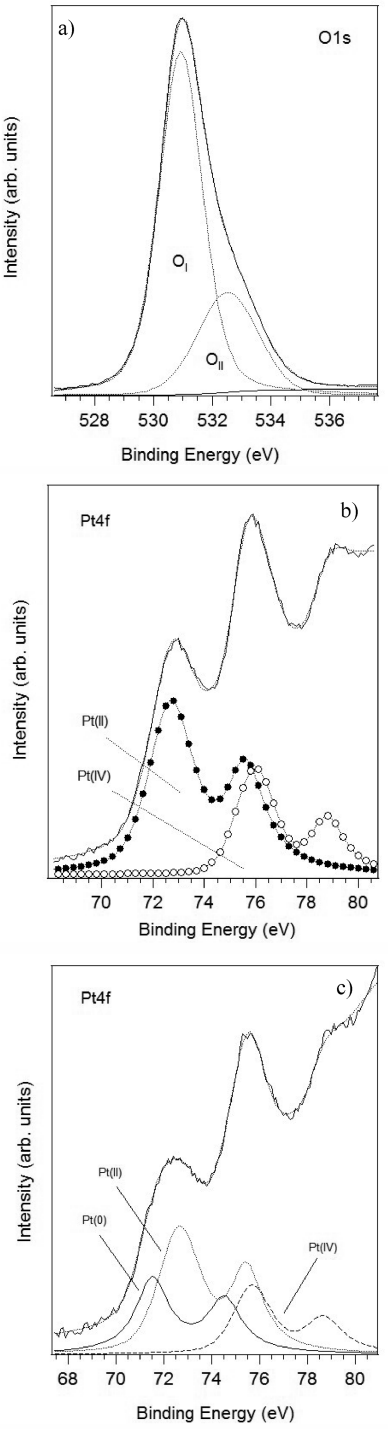

Figure 3. (a) XPS O1s spectrum of the Pt-SnO_2 inverted opal films after annealing in air at 773 K; (b) XPS Pt4f spectrum of the Pt-SnO_2 inverted opal films after annealing in air at 773 K. (c) Pt4f spectrum of the Pt-SnO_2 inverted opal film films after annealing in CO/Ar stream at 673 K. The different fitting components of peaks are also shown.

The analysis of the chemical composition showed that in inverted opal samples 2+ is the predominant platinum oxidation state, always coexisting with limited amounts of Pt(IV) species, at variance to sol−gel films where Pt(IV) is prevailing.[7,11] Therefore, it seems that the noble metal precursor is more resistant to oxidation to Pt(IV) in the opal structure rather than in the conventional sol−gel films. This may be due to the initial presence of the polystyrene

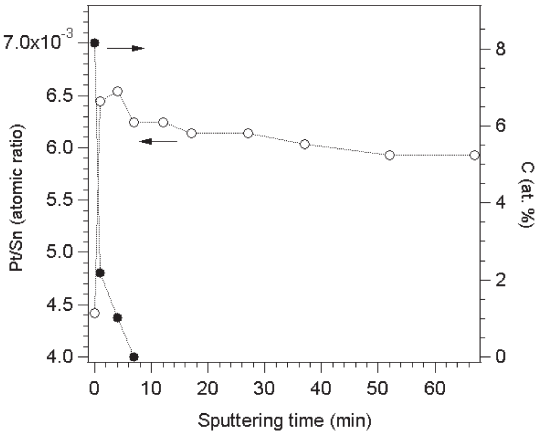

Figure 4. XPS depth profile for the Pt-doped SnO_2 film annealed in air. The Pt/Sn atomic ratio and C at % are reported as a function of the etching time.

template, which induces a reducing environment around platinum centers during the final thermal annealing.

The effective dispersion of Pt inside the host oxide was investigated by XPS depth profiling (Figure 4). In both air-annealed and CO-annealed films, the presence of Pt was detected throughout the film thickness with a homogeneous distribution in the investigated depth. Whereas a depletion of the platinum content was observed on the SnO_2 films surface, the typical average Pt/Sn atomic ratio is ~0.006 within the layers, which corresponds to about one-fourth of the nominal value.

A further important aspect is related to the purity of the samples. As a matter of fact, the C1s signal is detected only on the outer layers of the films (Figure 4), because of adventitious surface contamination, and it completely disappears after the first minutes of sputtering. This feature indicates that after the thermal treatment, all carbon-related species are efficiently removed from the samples.

3.3. Electrical Measurements. Aiming to use the obtained materials for environmental monitoring applications, the doped and undoped tin dioxide films were tested with a CO/Air gas mixture (72.5−580 ppm), and the working temperature was varied through a selected range. Figure 5a reports the resistance variation for Pt-doped SnO_2 inverted opal film at 623 K when pulses of the target gas (CO/air) with known CO concentration (580 ppm) were introduced in the measuring chamber, alternating with air pulses.

The resistance in the sensing layers regularly decreases under the reducing gases and increases under air, thus confirming the n-type semiconductor behavior of the oxide.

The sensing experiments were carried out in a temperature range between 523 and 623, K in order to determine the optimum working temperature. The relative response (R_{air}/R_{mix}) of Pt-doped SnO_2 inverted opal film (Figure 5 b) increases with temperature and becomes stationary at temperature above 573 K. The behavior resulted reproducible for all the obtained films.

Figure 6a illustrates the dynamic response of the Pt-doped tin oxide inverted opal sample under pulses having

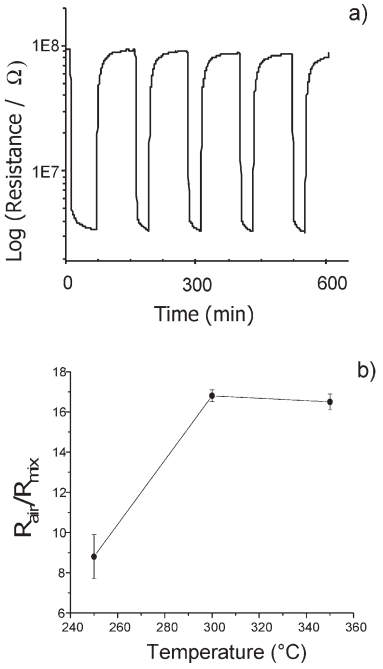

Figure 5. (a) Resistance variation for Pt-doped SnO_2 inverted opal films after exposure to pulses of CO (580 ppm)/air and air at 623 K. (b) Variation in the relative response of the sensor as a function of temperature.

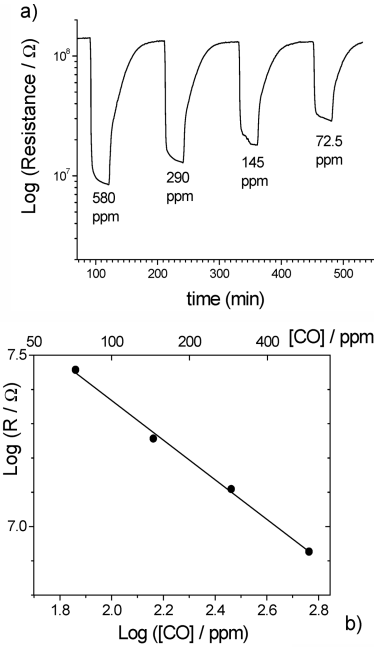

Figure 6. (a) Resistance variation for Pt-doped SnO_2 inverted opal film after exposure to pulses of CO/air at different CO concentrations at 623 K. (b) Variation in the relative response of the sensor as a function of CO concentration.

72.5, 145, 290, and 580 ppm CO concentration at a 623 K working temperature.

The variation in electrical resistance of the inverted opal sensor *vs*. CO concentration, drawn as log−log plot, is reported in Figure 6 b. Increasing the CO concentration increases the response of the sensing layer. The relationship is linear (R^2 = 0.9953 and slope ~0.5), and the electrical resistance changes by a factor of 4, changing the CO concentration by 1 order of magnitude.

This trend can be related to a conductance model limited by the electron transport across the intergranular Schottky barrier,[14] where

$$\sigma \propto \exp[-eV_s/kT] \quad (4)$$

(σ is the conductance and eV_s represents the surface barrier height at the intergranular contact). According to this model, the response of inverse opal-based gas sensors can be explained by using the following equation[2a,b,14c]

$$\sigma/\sigma_0 = A_g {p_g}^{\beta} \quad (5)$$

where σ_0 denotes the conductance in the absence of the target gas, p_g is the gas partial pressure, A_g is a prefactor, and the exponent β is the response order.

The value of β is dependent on the charge of the surface species and the stoichiometry of the pertinent oxidation − reduction surface reaction,[2a] moreover, it is strictly related to the microstructure of the material. As reported by Ozin et al.,[2b] a β value of 0.5 is indicative of a fully regular microstructure of the nanoparticles, as in the inverted opal. The presence of disordered microstructure is expected to increase β above this value, whereas local agglomeration or zones of the structure that result in it being less gas sensitive than others cause a reduction of β below this value.[2a]

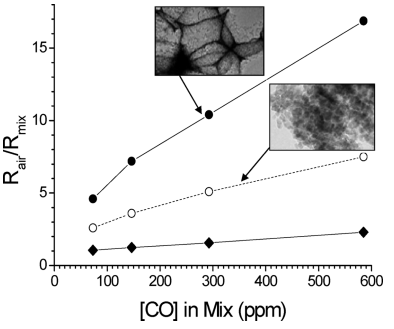

Figure 7. Variation in the relative response of the sensor as a function of CO concentration at 623 K for Pt-doped SnO_2 inverted opal (●); Pt-doped SnO_2 sol−gel (○); SnO_2 inverted opal (♦) films. In the insets, HRTEM micrographs of inverted opal and sol−gel Pt-doped SnO_2.

In our case, from the log−log plot, a β value of ~0.5 was deduced; this is in agreement with the regular array of cassiterite nanoparticles found in the inverse opal structure (see TEM micrographs, Figure 2c, d).

To demonstrate the sensitizing activity of the noble metal, the electrical responses *S* of undoped and Pt-doped SnO_2 opal films under the operative conditions described above (i.e., to 72.5, 145, 290, 580 ppm concentration pulses of CO at 623 K) are reported and compared in Figure 7.

Pt-doped SnO_2 films have higher sensitivity with respect to undoped SnO_2 at each CO concentration. In

(14) (a) Clifford, P. K.; Tuma, D. T. *Sens. Actuators* **1983**, *3*, 120. (b) Schierbaum, K. D.; Weimar, U.; Göpel, W. *Sens. Actuators, B* **1991**, *3*, 205. (c) Park, C. O.; Akbar, S. A. *J. Mater. Sci.* **2003**, *38*, 4611–4637.

particular, when using 580 ppm of CO, the electrical response is more than 1 order of magnitude higher in doped films. Pt doping does not significantly affect the working temperature when compared with undoped SnO_2.

To better investigate the structure−function relationship of the SnO_2 inverted opals for gas-sensing materials, we compared their electrical sensitivity with that of sol−gel (PS absent) nanostructured Pt-doped SnO_2 films, obtained by a similar procedure. Significantly, the opals showed higher sensitivity. All the electrical measurements were fully reproducible, and these performances result from the very high accessibility to gas transportation because of macro/meso internal porosity and from the fast transfer of electrons due to interconnection of nanocrystalline grains.

4. Conclusions

With reference to the results reported in the present paper and looking at the introductory objectives, we can suggest the following:

(1) Pure and Pt-doped SnO_2 inverted opals with remarkable order and regular macro- and mesoporosity were obtained by a one-step process, by a fast preparation route.

(2) The array is made by strictly interconnected nanoparticles with uniform size (∼5 nm), which favors the electrical transport across the material.

(3) Platinum is present as dopant in the inverse opal oxide films with homogeneous in depth distribution. The dominant oxidation state for the noble metal is Pt(II), although Pt(IV) species were also detected. Conversely, in the oxide layers prepared by the conventional sol−gel route, the latter component is prevalent.

(4) The electrical sensitivity of inverted opal-based films is enhanced by Pt doping and it can be suggested that the increased porosity and the electronic sensitization due to the dopant have a synergistic effect in enhancing the electrical response of opal films.

(5) The conductance regime of the doped-oxide opal film, obtained by the one step preparation, is indicative of a regular array of SnO_2 nanoparticles, without aggregation or disordered zones, as already reported by Ozin[2a,b] for the undoped tin oxide inverse opal by two steps process. This confirms the efficiency of the inverted opal architecture in the sensing process and demonstrates that Pt doping has no detrimental effect on the regular microstructure of the nanoparticles

Acknowledgment. The Milano group gratefully acknowledges the financial support of the Cariplo Foundation of Milano. The authors also thank Dr. Paolo Gentile for his assistance with SEM measurements. L.A. acknowledges the following Italian projects: MSE Industria 2015 ALADIN, Fondazione CARIPARO, Progetti di Eccellenza 2006 (Multilayer optical devices based on inorganic and hybrid materials by innovative synthetic strategies) and CNR-INSTM PROMO.